



# Anisotropy of soil water diffusivity of hillslope soil under spruce forest derived by X-ray CT and lab experiments

Steffen Beck-Broichsitter<sup>1</sup> · Jaromir Dusek<sup>1</sup> · Tomas Vogel<sup>1</sup> · Rainer Horn<sup>2</sup>

Received: 3 January 2022 / Accepted: 2 July 2022 / Published online: 17 September 2022  
© The Author(s) 2022

## Abstract

The idea of the study is to indicate direction-dependent differences in hydraulic conductivity,  $K(\theta)$ , and soil water diffusivity,  $D(\theta)$ , as function of the volume fraction related to the fractional capillary potential for each of the characteristic pore size classes by extended anisotropy factors. The study is exemplary focused on a BwC horizon of a Dystric Cambisol under spruce forest formed on the weathered and fractured granite bedrock in the mountainous hillslopes Uhlirška catchment (Czech Republic). Thus, undisturbed soil samples were taken in vertical ( $0^\circ$ ,  $y=x$ -axis) and horizontal ( $90^\circ$ ,  $z$ -axis) direction. The  $D(\theta)$  values and especially the  $D(\theta)$ -weighted anisotropy ratios showed that anisotropy increases with the volume fraction of macropores, MaP ( $d > 0.03$  mm), with  $r^2$  between 0.89 and 0.92. The X-ray computer tomography (CT) based anisotropy ratio ( $A_{CT}$ ) is larger for the horizontal sampled soil core with 0.31 than for the vertical with 0.09. This underlines the existence of a predominantly horizontally oriented pore network and the fact that weathered bedrock strata can initiate lateral preferential flow. The study results suggest that combining the hydraulic conductivity as intensity and the capacity parameter by means of diffusivity results in an extended anisotropy ratio which unveils the role of the soil hydraulic characteristics in generation of small-scale lateral preferential flow. In future, the small-scale direction-dependent differences in the soil hydraulic capacity and intensity parameter will be used for model-based upscaling for better understanding of preferential flow at the catchment scale.

**Keywords** Soil water diffusivity · Diffusivity-dependent anisotropy · X-ray CT · CT-based anisotropy

## Introduction

Soils generally consist of several and differently structured horizons and present direction-dependent properties due to the textural composition and this soil aggregate formation (Horn and Kutilek 2009; Alaoui et al. 2011). Its physical properties may vary from one location to another (heterogeneity), as well as from one direction to another at the same location (anisotropy). Even in the same layer, the heterogeneous arrangements of soil particles and aggregates due to anthropogenic and pedogenetic effects result in the

discrepancy of pore continuity and tortuosity between the different directions (Dörner and Horn 2009; Beck-Broichsitter et al. 2020a). The directional behaviour (isotropy or anisotropy) governs not only hydrologic processes (e.g., infiltration, recharge) but also soil aeration and root growth (Beck-Broichsitter et al. 2020c; Zhang and Peng 2021).

The saturated hydraulic conductivity,  $K_s$ , and the corresponding soil water diffusivity are of primary importance in analysing rates and directions of water flow and solute transport in the vadose zone in agricultural and forest hillslope catchments (Weiler and McDonnell 2007; Dohnal et al. 2012; Horn et al. 2014; Dusek and Vogel 2018). It is important to note that analysis of soil hydraulic properties on the catchment scale are regularly expensive and time consuming. Thus, experiments on the small-scale (e.g., soil pits) for determining  $K_s$  values are preferably used for model-based upscaling (Weiler et al. 2003; Dusek and Vogel 2016). The method of upscaling is associated with uncertainties and limited significance in heterogeneous catchments and hillslopes, although large-scale experiments represent an

✉ Steffen Beck-Broichsitter  
s.beck-broichsitter@soils.uni-kiel.de

<sup>1</sup> Department of Hydraulics and Hydrology, Faculty of Civil Engineering, Czech Technical University in Prague, Thakurova 7, 166 29 Prague, Czech Republic

<sup>2</sup> Institute of Plant Nutrition and Soil Science, Christian-Albrechts-University Kiel, Herrmann-Rodewald-Str. 2, 24118 Kiel, Germany

efficient way to obtain directional soil hydraulic properties functionally averaging local heterogeneities (e.g., Brooks et al. 2004; Pirastru et al. 2017). Other studies found that the occurrence of preferential flow in hillslope catchments are governed by small-scale soil structures (Carminati et al. 2007; Wiekenkamp et al. 2016). These local differences can be caused by tree roots, biopores, (Dohnal et al. 2012), shrinkage cracks and differently sized stones (Dusek and Vogel 2019), and tree- and machinery induced layering through compaction (Godefroid and Koedam 2010; Beck-Broichsitter et al. 2020b,c).

The X-ray computed tomography ( $\mu$ CT) is used to obtain 3D images and visualize the distribution and morphology of soil macropore networks and its characteristics (i.e., connectivity) for analysing local flow processes in macropores (i.e., Chandrasekhar et al. 2019; Leue et al. 2020; Schlüter et al. 2020). By contrast, additional methods as for example the scanning electron microscope (SEM) technique are more suitable for analysing the microstructure of soils in high-resolution including anisotropy and spatial variability of the permeability in unsaturated soils (Xu et al. 2020, 2021). Comparing both techniques, the  $\mu$ CT scanner was the method of choice with focus on the macropore network of undisturbed soil samples with a volume of 280 cm<sup>3</sup>.

The current study shows by means of a concrete example small-scale direction-dependent differences of a BwC horizon of a Dystric Cambisol under spruce forest formed on the weathered and fractured granite bedrock in the mountainous hillslopes Uhlirska catchment (Czech Republic). The idea of the study is to combine the soil capacity-related volume fraction of the pore classes,  $h(\theta)$ , with the intensity-related hydraulic conductivity function,  $K(\theta)$ , through the soil water diffusivity,  $D(\theta)$ , and their direction-dependent behaviour by an extended anisotropy factor, i.e.,  $D(\theta)*A$ . The aim was to identify the effect of small-scale soil structures in terms of cracks and differently sized stones affecting the soil water diffusivity between the macropore and fine pore size range for better understanding of the process affecting subsurface lateral flow in a forest hillslope. As a working hypothesis, a pronounced impact of macropores and wide coarse pore size range on  $D(\theta)$  function was expected.

## Materials and methods

### Study site

The experimental headwater catchment Uhlirska is in the northern part of the Czech Republic at the Jizera Mountains (15°18'49"E, 50°49'26"N). The area of the catchment is around 1.78 km<sup>2</sup> (Fig. 1). The mean annual temperature is 4.7 °C and the mean annual precipitation is 1380 mm.

The elevation ranges from 779 m above the mean sea level at the closing profile to 886 m a.s.l. at the catchment divide; the average altitude is 822 m a.s.l. The catchment valley is formed by the Cerna Nisa stream and gentle slopes. The average length of the hillslopes is 450 m and the slope angle vary between 5 and 20% (Sanda and Cislerová 2009). The soils at hillslopes are shallow sandy loams classified as Cryptopodzols, Cambisols (Fig. 2), and Podzols (Sanda et al. 2014; Beck-Broichsitter et al. 2022). The catchment was deforested due to acid rain in the 1980s and 1990s and then reforested in 1995 by spruce monoculture (*Picea abies*). The catchment has been equipped with an extensive monitoring and sampling network (Sanda et al. 2014).

### Soil classification and basic soil characteristics

The hillslope soil is classified as Dystric Cambisol, formed on the weathered and fractured granite bedrock with AE/Bs/Bsw/BwC/C horizons (IUSS Working Group WRB, 2015). The disturbed and undisturbed soil samples were collected in September 2020 from one soil pit at the hillslope with a mean gradient of 14% (8°). Soil material of each horizon was also used to investigate the organic carbon (OC) content at 1200 °C and carbonate through Scheibler method. Soil texture (stones > 2 mm, sand: 0.063 mm to 2 mm; silt: 0.002 mm to 0.063 mm; clay: < 0.002 mm) was analysed by the combined sieve and pipette method with three repetitions each (Hartge and Horn 2016) and further classified by FAO (2006).

### Soil physical properties

In total, 24 stainless steel rings (280 cm<sup>3</sup>, height: 5.5 cm; diameter: 8 cm) of undisturbed soil samples were used, 12 for vertical (0°,  $y=x$ -axis) and horizontal (90°,  $z$ -axis) sampling direction, respectively (Fig. 2). The samples were taken from the BwC horizon in 0.35–0.50 cm depth. At laboratory, the sample rings were first carefully wetted for determining the saturated hydraulic conductivity,  $K_s$  (m s<sup>-1</sup>), and in a second step, the water retention curve and the unsaturated hydraulic conductivity,  $K(h)$ , were simultaneously determined. In a last step, the sample rings were dried for 24 h at 105 °C to determine the residual amount of water content,  $\theta_r$  (cm<sup>3</sup> cm<sup>-3</sup>), and the dry bulk density,  $\rho$  (g cm<sup>-3</sup>), respectively, while initial water content,  $\theta$  was determined by total water loss related to core volume.

The KSAT device (Meter Group AG, Munich, Germany) was used to derive the  $K_s$  values based on the German method standards (DIN 18130-1 1998). The  $K_s$  values were determined in the falling head mode and fitted by an exponential function using the KSAT VIEW software version 1.5.0 (Meter Group AG, Munich, Germany):

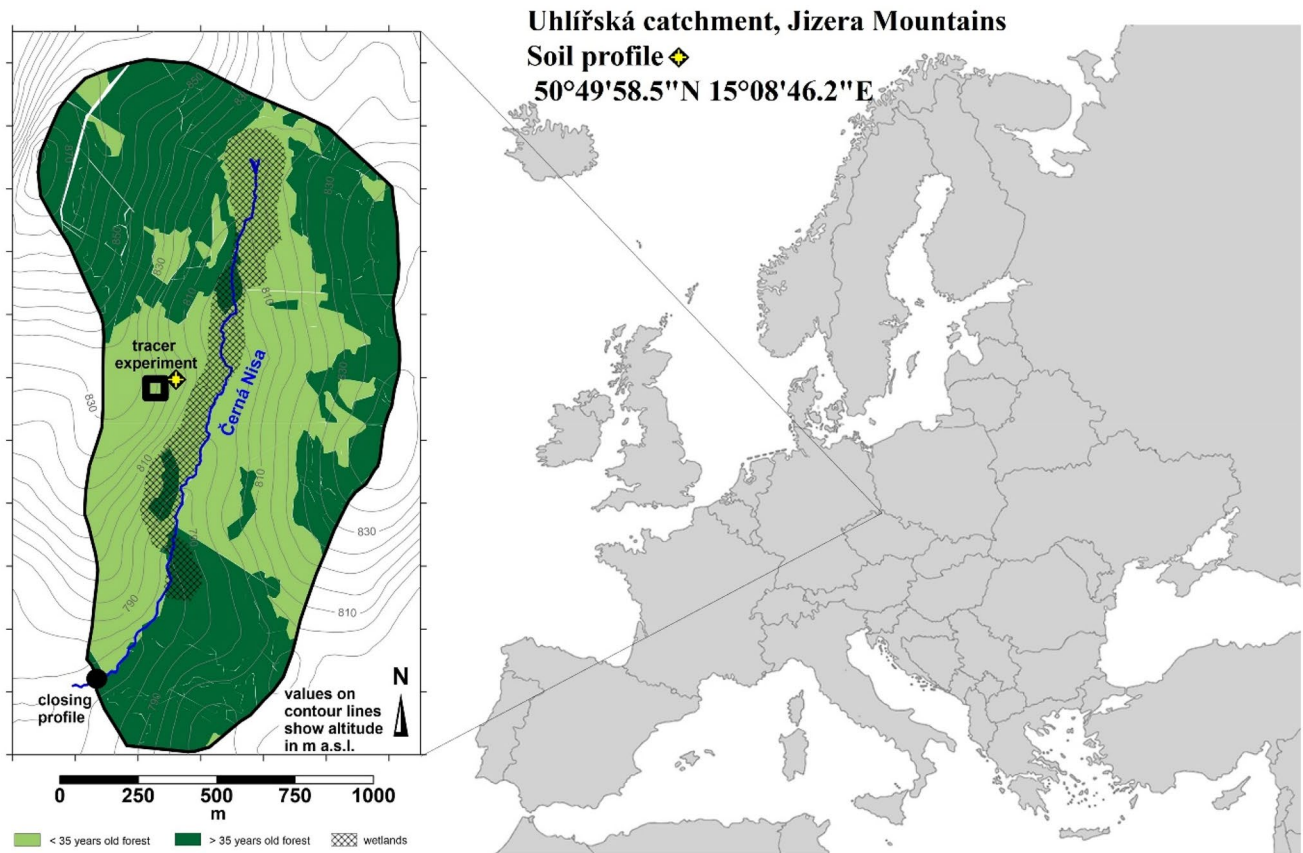


**Fig. 1** Scheme of Uhlířská catchment, Jizera Mountains (15°08'46.2"E, 50°49'58.5"N), Czech Republic. Modified after Sanda et al. (2014). Map of Europe (open source: Eurostat)

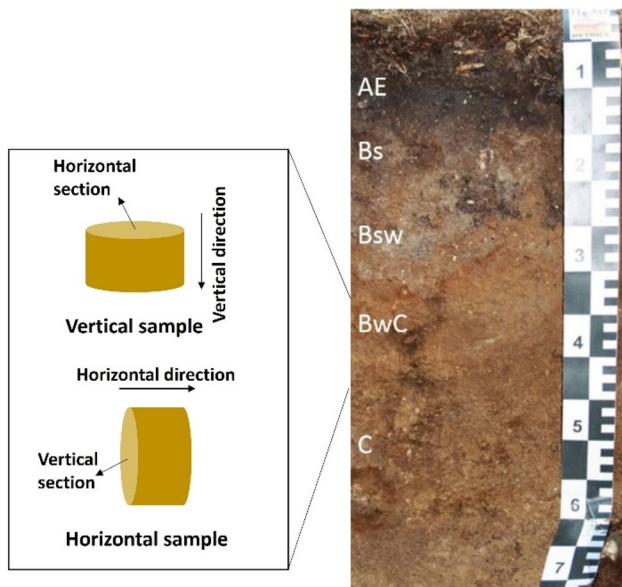


**Fig. 2** Dystric Cambisol with AE/Bs/Bsw/BwC/C horizons located in the Jizera Mountains in northern Bohemia in the Czech Republic (Photo by M. Leue). Undisturbed soil cores in vertical (0°, y=x-axis) and horizontal (90°, z-axis) sampling direction

$$h(t) = h_0 \exp\left(-Ks \cdot \frac{A_{bur}}{A_{sample}} \cdot \frac{1}{L} \cdot t\right) = a \exp(-b \cdot t) + c, \tag{1}$$

where  $h(t)$  is the pressure head (cm) at a certain time,  $t(s)$ ,  $h_0$  is the pressure head at  $t=0$ ,  $A_{bur}$  is the cross-sectional area of the burette (4.524 cm<sup>2</sup>),  $A_{sample}$  is the cross-sectional area of the soil sample (50 cm<sup>2</sup>),  $L$  is the length of the soil sample (5 cm),  $Ks$  is the saturated hydraulic conductivity (cm s<sup>-1</sup>), and  $a$  (cm),  $b$  (s<sup>-1</sup>), and  $c$  (cm) are the fitting parameters of the fitted exponential pressure head function.

The HYPROP measurement device (Meter Group AG, Munich, Germany) was used for simultaneous determination of the soil water retention curve and the hydraulic conductivity function (Schindler et al. 2010) using the extended evaporation method (Schindler 1980). The wetted sample rings were placed on the HYPROP base containing two vertically installed tensiometer at 1.25 cm and 3.75 cm distance from the bottom, both sealed at the bottom and placed on a balance (UMS GmbH Munich 2015). The sample mass changes (g) and pressure (hPa) in intervals of 10 min were automatically recorded by HYPROP-VIEW software version 1.4.0 (Meter Group AG, Munich, Germany). The samples dried out to

about -600 hPa (lower tensiometer) and -850 hPa (upper tensiometer).

The  $h$  values at the upper,  $h_u(t)$ , and the lower,  $h_l(t)$ , tensiometer were used to determine the hydraulic gradient,  $i_m$  ( $\text{cm cm}^{-1}$ ), per time interval,  $\Delta t = t_0 - t_1$ , along the horizontal distance,  $\Delta z$ , between both tensiometer (Schindler 1980; Wendroth et al. 1993):

$$i_m = \frac{1}{2} \left( \frac{h_u(t_0) - h_l(t_0)}{\Delta z} + \frac{h_u(t_1) - h_l(t_1)}{\Delta z} \right) - 1. \tag{2}$$

The  $K(h)$  values were calculated according to the Darcy–Buckingham law (Schindler 1980; Wendroth et al. 1993):

$$K(h^*) = \frac{\Delta m}{\alpha A_{\text{sample}} \cdot \rho_{\text{H}_2\text{O}} \cdot \Delta t \cdot i_m}, \tag{3}$$

where  $h^*$  (hPa) is the mean value of the pressure heads of the two tensiometer (i.e.,  $h^* = 0.5(h_u + h_l)$ ) with  $\Delta t = 10$  min,  $\Delta m$  is the sample mass difference (g) in the time interval,  $\alpha$  is a flux factor (-),  $\rho_{\text{H}_2\text{O}}$  is the density of water ( $\sim 1 \text{ g cm}^3$ ).

The data points of the soil water retention curve were calculated based on the water loss per volume of the sample and the corresponding geometric mean tension of the sample in the same time interval (UMS GmbH Munich 2015). Pressure chamber was used to determine moisture content at  $h$  value of -15,000 hPa.

The HYPROP-Fit software was used for calculation, evaluation, and fitting of the observed  $h(\theta)$  and  $K(h)$  functions of the vertical and horizontal samples. The observed water retention data were fitted with the constraint unimodal (van Genuchten 1980) and bimodal van Genuchten model (Durner 1994):

$$\text{Se}(h) = \frac{\theta - \theta_r}{\theta_s - \theta_r} = \begin{cases} \sum_{i=1}^2 w_i [1 + (\alpha_i h)^{n_i}]^{-m_i} & \text{for } |h| < 0 \\ 1 & \text{for } |h| \geq 0 \end{cases}, \tag{4}$$

where  $\text{Se}(h)$  is the effective saturation (-),  $\theta_s$  is saturated and  $\theta_r$  is residual water content, respectively,  $\alpha$  ( $\text{cm}^{-1}$ ),  $n$  (-) and  $m$  (-), with  $m = 1 - 1/n$ , are empirical van Genuchten fitting parameters for both pore domains (index  $i$ ), and  $w_i$  is a pore-domain weighting factor (bimodal:  $w_1 = 1 - w_2$ , unimodal:  $w_2 = 0$ ).

The unsaturated hydraulic conductivity,  $K(\text{Se})$  was determined as function of the effective saturation with the combined Mualem–van Genuchten type analytical function and the bimodal retention function (Priesack and Durner 2006):

$$K(\text{Se}) = K_s \left( \sum_{i=1}^k w_i \text{Se}_i \right)^\tau \left( \frac{\sum_{i=1}^k w_i \alpha_i [1 - (1 - \text{Se}_i^{1/m_i})^{m_i}]}{\sum_{i=1}^k w_i \alpha_i} \right)^2, \tag{5}$$

where integer  $k$  denotes the modality of the model (i.e.,  $k = 2$  for bimodal),  $w_i$  is a weighting factor for the sub-curves of each pore domain ( $0 < w_i < 1$  and  $\sum w_i = 1$ ), and  $\tau$  (-) is the tortuosity.

In a first step, the water retention function was fitted as well as the derived fitting parameters  $\alpha_i$ ,  $n_i$ ,  $m_i$ , which were then used in a second step for fitting the  $K(\text{Se})$  functions.

The most appropriate soil water retention model is selected by the second-order Akaike Information Criterion (Hurvich and Tsai 1989) was used. The error between fitted and observed  $K(\text{Se})$  values is automatically determined by the root mean square error (RMSE) through HYPROP-Fit software.

The pore size distribution (PSD) was calculated by the slope of the water retention curve  $\Delta \text{Se} / \Delta h$ . The  $h$  value of -10 hPa (about 9.81 cm) was assumed as boundary between the macropores MaP ( $h_1 \geq -10$  hPa), structural pores: wide coarse pores wCP ( $-10 > h_2 \geq -60$  hPa), and textural pores: narrow coarse pores nCP ( $-60 > h_3 \geq -300$  hPa), medium pores MP ( $-300 > h_4 \geq -15,000$  hPa), and fine pores FP ( $h_5 < -15,000$  hPa) assumed from the peaks in the PSD at an equivalent pore diameter (Beck-Broichsitter et al. 2020a,b). The pore diameter for the different pore size classes were calculated as (Hartge and Horn 2016)

$$r_i = \frac{0.149}{|h_i|}, \tag{6}$$

where  $r_i$  is the pore radii (cm) and  $h$  is the pressure head (cm), assuming 1 cm is proportional to -1 hPa, for the  $i$ th pore size class: MaP ( $h_1 \geq -10$  hPa), wCP ( $-10 > h_2 \geq -60$  hPa), nCP ( $-60 > h_3 \geq -300$  hPa), MP ( $-300 > h_4 \geq -15,000$  hPa), and FP ( $h_5 < -15,000$  hPa). Using the Laplace equation for a capillary rise, these five pore classes can be defined with pore diameter  $d$  as: MaP with  $d > 0.3$  mm, wCP with  $0.3 \geq d > 0.05$  mm, nCP with  $0.05 \geq d > 0.01$  mm, MP with  $0.01 \geq d > 0.0002$  mm, and FP with  $d \leq 0.0002$  mm.

The anisotropy ratio (AR) is defined as ratio of  $K(\text{Se})$ -values obtained in horizontal (hor) and vertical (ver) direction (Beck-Broichsitter et al. 2020a, b):

$$\text{AR} = \frac{K(\text{Se})_{\text{hor}}}{K(\text{Se})_{\text{ver}}}, \tag{7}$$

where the subscripts ver and hor indicate  $K(\text{Se})$  values obtained from cores sampled in vertical and horizontal directions, respectively.

The soil water diffusivity,  $D(\theta)$ , is used for linking the intensity parameter with the capacity-based volume fraction of  $i$ th pore size classes with a pore size-related fraction of the capillary potential (Beck-Broichsitter et al. 2020a). The  $D(\theta)$  ( $\text{cm}^2 \text{ d}^{-1}$ ) corresponds to the product of the  $K(\theta)$  and the differential inverse water capacity,  $dh/d\theta$  (Hillel 1998):

$$D(\theta) = K(\theta) \frac{dh}{d\theta}, \quad (8)$$

The effective  $D(\theta)$  values for the  $i$ th pore size classes were calculated as (Beck-Broichsitter et al. 2020a)

$$D_i(\theta_i) = \int_{\theta^+}^{\theta^-} K(\theta_i) \frac{dh}{d\theta_i} d\theta, \quad (9)$$

where  $\theta^+(h^+)$  is the upper and  $\theta^-(h^-)$  is the lower value of each of the five  $h$ -ranges defined above.

A diffusivity-dependent effective value of the anisotropy ratio  $AR_{D(\theta)}$  ( $\text{cm}^2 \text{d}^{-1}$ ), per pore size class  $i$  was calculated as (Beck-Broichsitter et al. 2020a)

$$AR_{D(\theta)} = D_i(\theta_i) \int_{\theta^+}^{\theta^-} \frac{1}{AR_i} d\theta. \quad (10)$$

The diffusivity-dependent anisotropy is a direct link between intensity and capacity parameters and improves the information about the impact of the pore size classes on  $K_s$  and finally  $D(\theta)$  values (Beck-Broichsitter et al. 2020a).

## X-ray computer tomography

Internal structure of the two field moist undisturbed soil samples in stainless steel cores ( $280 \text{ cm}^3$ , height: 5.5 cm; diameter: 8 cm) (withdrawn in vertical and horizontal direction) with volume size of  $1741 * 1854 * 1621$  voxel was visualized by X-ray computer tomography (CT). The CT images were obtained using a GE vltomelx M 300  $\mu$ CT scanner at the Technical University in Brno (Czech Republic). The X-ray photon energy was set to 220 keV with a current of 300  $\mu$ A (GE Sensing & Inspection Technologies GmbH, Wunstorf, Germany). A 1-mm Cu pre-filter was used to minimize beam hardening. Each soil sample was scanned in two height steps resulting in two overlapping 3D image data sets that were subsequently reconstructed to obtain a single 3D core volume. For reconstruction, the software datoslx, version 1.5.0.15 (GE Sensing Technologies) was used, which is based on a modified Feldkamp algorithm (Feldkamp et al. 1984). A spatial resolution in terms of an isotropic voxel edge length of 55  $\mu\text{m}$  was achieved for both samples.

The image pre- and post-processing was done with the SoilJ software (Koestel, 2018) implemented as plugin for the open-source software ImageJ 1.x (Schneider et al. 2012). About 2 mm of the outermost layer of the soil samples were clipped out by image grayscaleing to remove the cylinder wall to calculate the bulk density of the region of interest (ROI). This information can also be used for SoilJ's beam-hardening correction routine to remove scattering artifacts from images of steel rings (Hansson et al. 2017).

SoilJ offers image segmentation options as well as the possibility of analysing joint histograms of several calibrated images (Koestel 2018) and for the binarization of the gray value images, a global threshold was calculated for each of the 403 slices per soil core ( $ROI_{\text{vertical}}$ ) and 407 slices per soil core ( $ROI_{\text{horizontal}}$ ), using Otsu's method (Otsu 1979). Histograms of objects volumes (e.g., pores, soil matrix, stones) were used to determine thresholds between the pore volume classes (Pagenkemper et al. 2013; Leue et al. 2020); objects with diameter of around 1.134 pixel were denoted as macropores ( $d > 0.3 \text{ mm}$ ).

The global morphological measures of the selected ROI (critical diameter and thickness of pores, macropore volume) were calculated in addition to the Minkowski functionals. For this purpose, SoilJ makes use of the algorithms included in the MorphoLibJ (Legland et al. 2016) and BoneJ (Doubé et al. 2010) packages.

To quantify the anisotropy and, therefore, the directionality of heterogenous structured materials, tensorial structural characteristics are needed to determine the degree of anisotropy and the preferred orientation. The mean intercept length (MIL) tensor is the most used technique for it (Odgaard 1997; Klatt et al. 2017) and the degree of the CT-based anisotropy ( $A_{\text{CT}}$ ) is defined as follows (Doubé et al. 2010):

$$A_{\text{CT}} = 1 - \frac{\text{Long axis eigenvalue}}{\text{Short axis eigenvalue}}, \quad (13)$$

where  $A_{\text{CT}} = 0$  means isotropic and  $A_{\text{CT}} = 1$  anisotropic condition, and the longest axis has the smallest eigenvalue.

The Paraview software version 5.9.2-RC2 (e.g., Ahrens et al. 2005) was used for visualisation of the macropore volumes ( $MaP_{\text{CT}}$ :  $d > 1.134$  pixel) of the vertical and horizontal sampled soil cores.

## Results and discussion

### Soil physical and chemical properties

The soil texture is classified as loam for the AE/Bs/Bsw horizons and sandy loam for the BwC horizon with clay contents between 110 and 120  $\text{g kg}^{-1}$  and stone contents between 87 and 240  $\text{g kg}^{-1}$  (Table 1). The pH values vary between 3.9 and 4.5, and the organic carbon content ranges from 35 in the BwC horizon to 65  $\text{g kg}^{-1}$  in the Bs horizon. The  $\rho$  values increase from 0.65 to 1.25  $\text{g cm}^{-3}$  with increasing soil depth.

The results in Table 2 show higher  $K_s$  values with 554  $\text{cm d}^{-1}$  for the horizontal direction compared to the vertical one with 123  $\text{cm d}^{-1}$  with  $\rho$  values of 1.23  $\text{g cm}^{-3}$ , respectively.

**Table 1** Soil physical and chemical properties of the AE/Bs/Bsw/BwC/C horizons of the Dystric Cambisol; organic carbon (OC) content,  $\text{pH}_{\text{CaCl}_2}$ , and soil texture, dry bulk density ( $\rho$ ); mean values and standard deviations (symbol  $\pm$ ) of three repetitions each, five for  $\rho$ 

Horizon	Depth (m)	Clay ( $\text{g kg}^{-1}$ )	Silt ( $\text{g kg}^{-1}$ )	Sand ( $\text{g kg}^{-1}$ )	Stones ( $\text{g kg}^{-1}$ )	OC ( $\text{g kg}^{-1}$ )	$\text{pH}_{\text{CaCl}_2}$ (-)	$\rho$ ( $\text{g cm}^{-3}$ )
AE	0–0.1	110 $\pm$ 15	350 $\pm$ 20	540 $\pm$ 15	145	44 $\pm$ 10	4.0 $\pm$ 0.4	0.65 $\pm$ 0.07
Bs	0.1–0.20	115 $\pm$ 20	430 $\pm$ 25	455 $\pm$ 25	194	65 $\pm$ 11	3.9 $\pm$ 0.3	0.77 $\pm$ 0.12
Bsw	0.20–0.35	110 $\pm$ 15	440 $\pm$ 30	450 $\pm$ 30	87	47 $\pm$ 7	4.5 $\pm$ 0.3	0.85 $\pm$ 0.01
BwC	0.35–0.50	120 $\pm$ 15	530 $\pm$ 25	330 $\pm$ 20	240	35 $\pm$ 7	4.3 $\pm$ 0.2	1.25 $\pm$ 0.18

**Table 2** Total porosity, TP ( $\text{cm}^3 \text{cm}^{-3}$ ) and volume fractions of pore classes for macropores MaP ( $h_1 \geq -10$  hPa), b) wide coarse pores wCP ( $-10 > h_2 \geq -60$  hPa), c) narrow coarse pores nCP ( $-60 > h_3 \geq -300$  hPa), d) medium pores MP ( $-300 > h_4 \geq -15,000$  hPa), and e) fine pores FP ( $h_5 < -15,000$  hPa)

Direction	TP ( $\text{cm}^3 \text{cm}^{-3}$ )	MaP ( $\text{cm}^3 \text{cm}^{-3}$ )	wCP ( $\text{cm}^3 \text{cm}^{-3}$ )	nCP ( $\text{cm}^3 \text{cm}^{-3}$ )	MP ( $\text{cm}^3 \text{cm}^{-3}$ )	FP ( $\text{cm}^3 \text{cm}^{-3}$ )	$K_s$ ( $\text{cm d}^{-1}$ )	$\rho$ ( $\text{g cm}^{-3}$ )
ver	0.463 $\pm$ 0.05	0.038 $\pm$ 0.002	0.073 $\pm$ 0.004	0.043 $\pm$ 0.002	0.082 $\pm$ 0.004	0.227 $\pm$ 0.009	123 $\pm$ 98	1.23 $\pm$ 0.065
hor	0.534 $\pm$ 0.07	0.079 $\pm$ 0.023	0.086 $\pm$ 0.005	0.053 $\pm$ 0.007	0.087 $\pm$ 0.018	0.229 $\pm$ 0.017	554 $\pm$ 243	1.23 $\pm$ 0.041

Saturated hydraulic conductivity,  $K_s$  ( $\text{cm d}^{-1}$ ), and dry bulk density,  $\rho$  ( $\text{g cm}^{-3}$ ) in vertical (ver) and horizontal (hor) direction; mean and standard deviations ( $\pm$  symbol) from 12 replicates

**Table 3** Root mean square error (RMSE) for mean deviation between the fitted and observed water content  $\theta$ , and the unsaturated hydraulic conductivity Log  $K(\text{Se})$ 

	ver	hor	AICc	ver	hor
$\theta$ ( $\text{cm}^3 \text{cm}^{-3}$ )	0.0012 $\pm$ 0.0005	0.002 $\pm$ 0.0008	Unimodal	- 1282 $\pm$ - 24	- 1379 $\pm$ - 119
Log $K(\text{Se})$ ( $\text{cm d}^{-1}$ )	0.1188 $\pm$ 0.089	1.148 $\pm$ 1.515	Bimodal	- 1537 $\pm$ - 138	- 1605 $\pm$ - 97

Values of the Akaike Information Criterion (AICc) from fitting uni- and bi-modal van Genuchten soil water retention models. Vertical (ver) and horizontal (hor) direction; mean and standard deviations ( $\pm$  symbol) from 12 replicates

**Table 4** Hydraulic parameter of the soil water retention data with bimodal van Genuchten model (Durner 1994) and bimodal unsaturated hydraulic conductivity  $K(\text{Se})$  (Priesack and Durner 2006) in vertical (ver) and horizontal (hor) direction; mean and standard deviations ( $\pm$  symbol) from 12 replicates

Direction	$\theta_r$ ( $\text{cm}^3 \text{cm}^{-3}$ )	$\theta_s$ ( $\text{cm}^3 \text{cm}^{-3}$ )	$\alpha_1$ ( $\text{cm}^{-1}$ )	$\alpha_2$ ( $\text{cm}^{-1}$ )	$n_1$	$n_2$	$w_2$	$\tau$	$r^2$
ver	0.224 $\pm$ 0.028	0.464 $\pm$ 0.002	0.002 $\pm$ 0.058	0.118 $\pm$ 0.065	1.766 $\pm$ 0.367	1.504 $\pm$ 0.135	0.724 $\pm$ 0.013	0.581 $\pm$ 1.548	0.994
hor	0.184 $\pm$ 0.019	0.543 $\pm$ 0.006	0.276 $\pm$ 0.099	0.0012 $\pm$ 0.018	1.402 $\pm$ 0.002	1.225 $\pm$ 0.072	0.191 $\pm$ 0.097	0.782 $\pm$ 2.541	0.991

The volume fractions of pore size tend to be higher for the horizontal than vertical collected samples, especially the volume fraction of macropores. MaP is more pronounced for the horizontal direction with 0.079  $\text{cm}^3 \text{cm}^{-3}$  than the vertical one with 0.038  $\text{cm}^3 \text{cm}^{-3}$ . With respect to the total porosity, the macropore volume is around 7.4% in vertical and 13.1% in horizontal direction (Table 2).

The RMSE values in Table 3 vary between 0.0012 and 0.002  $\text{cm}^3 \text{cm}^{-3}$  for  $\theta$  and between 0.1188 and 1.148  $\text{cm d}^{-1}$  for Log  $K(\text{Se})$ . The AICc values for the bimodal model are smaller (larger in absolute value) in both directions than for the unimodal model. Thus, the bimodal model is found to be provide more appropriate (Table 3).

The results in Table 4 indicate that the fraction of the second pore domain,  $w_2$ , representing the smaller pore size is notable higher in vertical direction with 0.724 than in horizontal direction with a more dominating larger pore size ( $1-w_2$ ) with 0.809.

The slopes of the soil water retention curves,  $\Delta Se/\Delta h$ , per interval in vertical and horizontal direction shown in Fig. 3c, indicate a structural peak at  $-10$  hPa. A more pronounced second matric peak at about  $-1000$  hPa is seen for the vertical direction (Fig. 3c), while the second matric peak for the horizontal direction at about  $-300$  hPa is less pronounced (Fig. 3d). Overlooking the bi-peak structure, the higher the amount of macropores and medium pores, the more pronounced is the structural peak as also mentioned in Ding et al. (2016) and Beck-Broichsitter et al. (2020b).

The results indicate that the used HYPROP measurement system is an appropriate tool for soils with bimodal pore size distribution (Durner 1994) considering two different flow domains: the macropore system and the soil matrix (Weninger et al. 2018). The direction-dependent differences in the pore size distribution as shown in Fig. 3c and d differ from the theory of isotropic capacity parameter as also

disproved by Horn et al. (2014). However, differences in the volume fraction of the pore classes and, therefore, the peak structure can be related to the small-scale heterogeneity in soil profiles (Horn et al. 2019; Beck-Broichsitter et al. 2020a, b). On the other hand, capturing a larger volume fraction of the pore classes is greater for vertically as compared to horizontal-oriented soil sampling (Beck-Broichsitter et al. 2020a).

### Unsaturated hydraulic conductivity and anisotropy ratio

The functions of  $K(S_e)$ , fitted with the bimodal model are shown in Fig. 4. The results show weak direction-dependent differences of  $K(S_e)$  between the two directions of sampling. The values of  $K(S_e)$  are slightly larger in horizontal than in vertical direction for saturated conditions ( $S_e$  ranging from 0.8 to 1).

The results in Table 2 indicate higher mean  $K_s$  values in horizontal ( $554 \text{ cm d}^{-1}$ ) than in vertical direction ( $123 \text{ cm d}^{-1}$ ) and in Fig. 5, the anisotropy ratio AR is shown as a function of pressure head. In the range of the

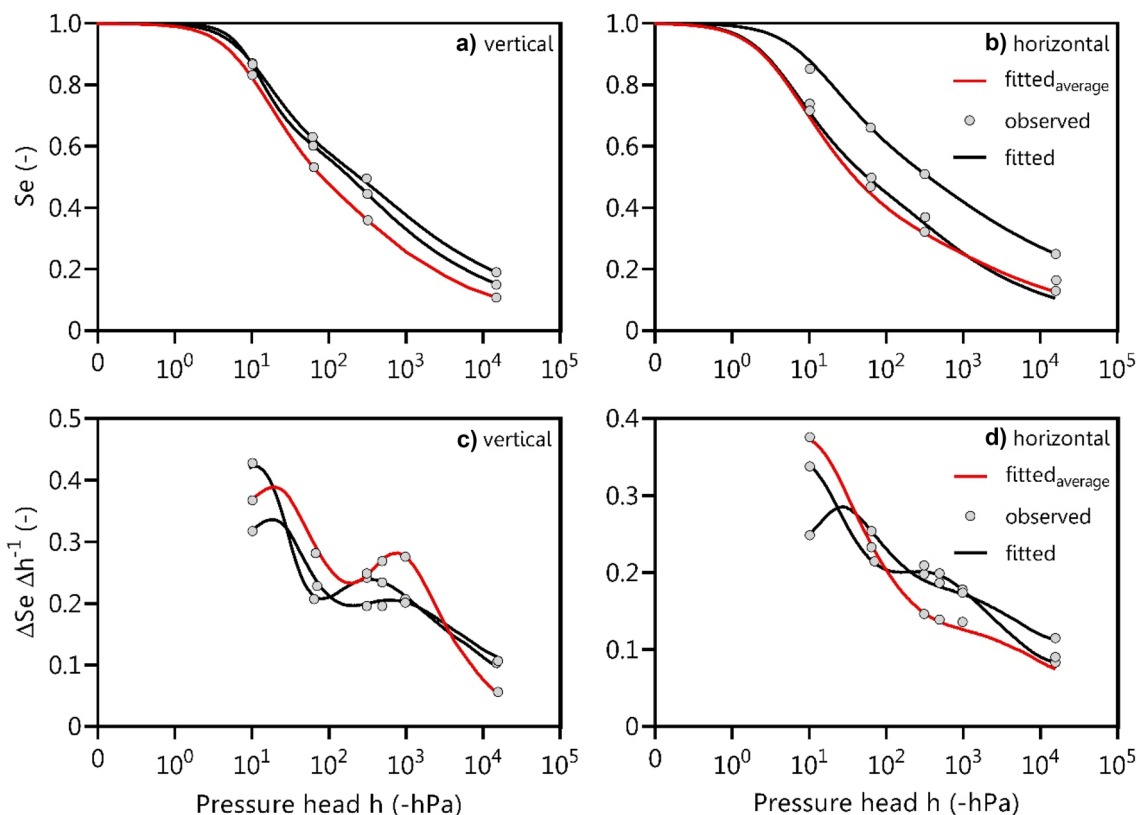


**Fig. 3** Soil water retention curves approximated parameter fits from the mean of 5 data points with HYPROP-Fit software of the average and two representative soil water retention data sets with bimodal ( $w_1=1-w_2$ ) constrained ( $m=1-n-1$ ) van Genuchten model (Durner

1994); corresponding relative pore volume fractions (1c,d) at the measured pressure head intervals in terms of the mean slope of the effective saturation ( $\Delta Se/\Delta h$ ) per interval in vertical and horizontal direction

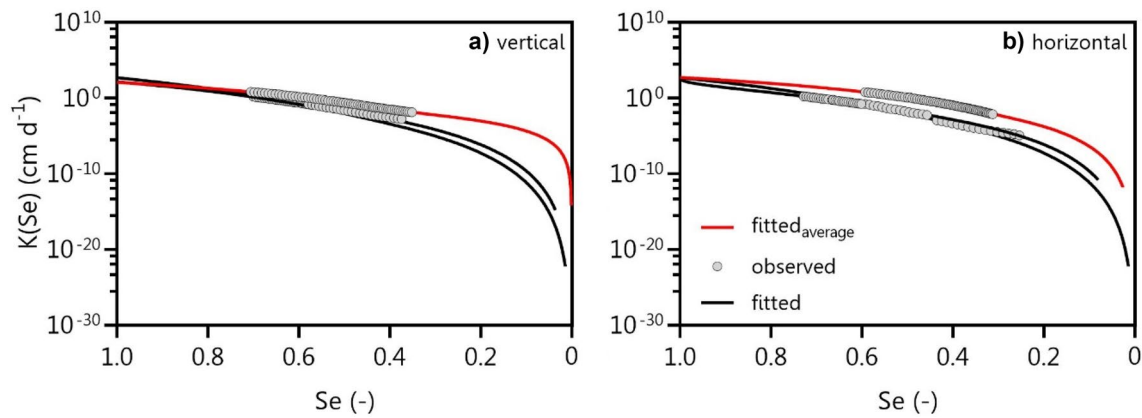


**Fig. 4** Functions of  $K(\text{Se})$  of the average and two representative  $K(\text{Se})$  functions with bimodal retention function in vertical and horizontal direction

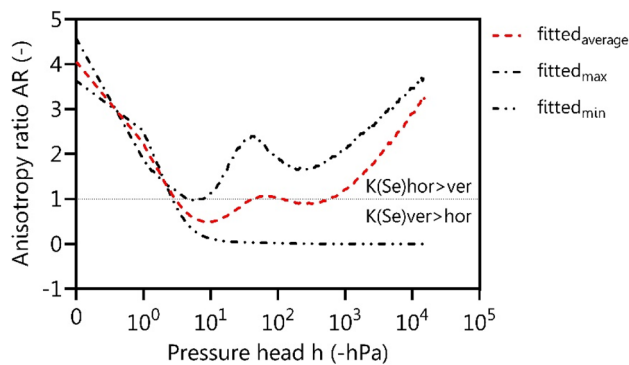


**Fig. 5** Average anisotropy ratio ( $K(\text{Se})_{\text{hor}}/K(\text{Se})_{\text{ver}}$ ) plus maximum  $\text{AR}_{\text{max}}$  (highest  $K(\text{Se})_{\text{hor}}/K(\text{Se})_{\text{ver}}$ ) and minimum  $\text{AR}_{\text{min}}$  (lowest  $K(\text{Se})_{\text{hor}}/K(\text{Se})_{\text{ver}}$ ) from 12 replicates each as function of the pressure head

macropores ( $h \geq -10$  hPa), the AR values decrease from 4.6 to 0.3. With the emptying of the soil pores, the AR values increase and peak at about  $-60$  hPa. The values of AR increase up to 3.5 in the unsaturated conditions.

The anisotropy ratio of 4.5 at saturated conditions suggests an increased potential for lateral flow above a less permeable bedrock. Predominantly horizontal-oriented pore network was created by plant roots and root fragments (Sanda and Cislerová 2009; Dohnal et al. 2012), and differently sized stones and rock fragments (Dusek and Vogel 2019). This assumption is further underlined by a macropore volume of 8.2% in vertical and 14.8% in horizontal direction (Table 2).

As recently mentioned, the anisotropy of hydraulic conductivity is often neglected, because it can only partially explain the complex variably saturated response dynamics in layered hillslope soils (Mirus 2015).

### Soil water diffusivity

The functions of soil water diffusivity  $D(\theta)$  for the volume fraction of the pore classes show that the function of  $D(\theta)$  has a positive slope for the macropores and wide coarse pores with an  $r^2$  between 0.66 and 0.84 for both sampling directions (Fig. 6). On the other hand, the narrow coarse pores, medium pores, and fine pores show less pronounced positive and also negative linear regressions with  $r^2$  between 0.29 and 0.44.

In Fig. 7, the  $D(\theta)$ -weighted anisotropy ratios  $\text{AR}_{D(\theta)}$  defined in Eq. 10 are depicted. The results show a positive linear relationship for the MaP ( $r^2$  of 0.89–0.92) and wCP ( $r^2$  of 0.49–0.61), while nCP, MP, and FP indicate a negative linear relationship ( $r^2$  of 0.28–0.52). Thus, the anisotropy ratios  $\text{AR}_{D(\theta)}$  strongly increases with the volume fraction of macropores and wide coarse pores, respectively.

The linear regression between  $D(\theta)$  and the diffusivity-dependent effective value of the anisotropy ratio,  $\text{AR}_{D(\theta)}$ , for the narrow coarse to fine pore range shows  $r^2 < 0.52$  (Fig. 7). Thus, intensity parameters are also functions of pore continuity and connectivity and not directly of capacities (Horn et al. 2009, 2014) as exemplary shown in Fig. 8.

The  $K(\text{Se})$ - and, therefore, the  $D(\theta)$  values are mostly related to the  $K$ s values (Germer and Braun 2015) and the volume fraction of the macropores and wide coarse pores (Beck-Broichsitter et al. 2020a, b). The higher van Genuchten parameter  $n_1$  and  $n_2$  in vertical direction (1.766 and 1.504) than  $n_1$  and  $n_2$  in horizontal direction (1.402 and 1.225, see Table 4) indicate a lower water capillary adsorption capacity for the macropores and the coarse to medium pores in vertical compared to horizontal direction. As a result, a more pronounced drop in conducting water when drained is observed for vertical than horizontal



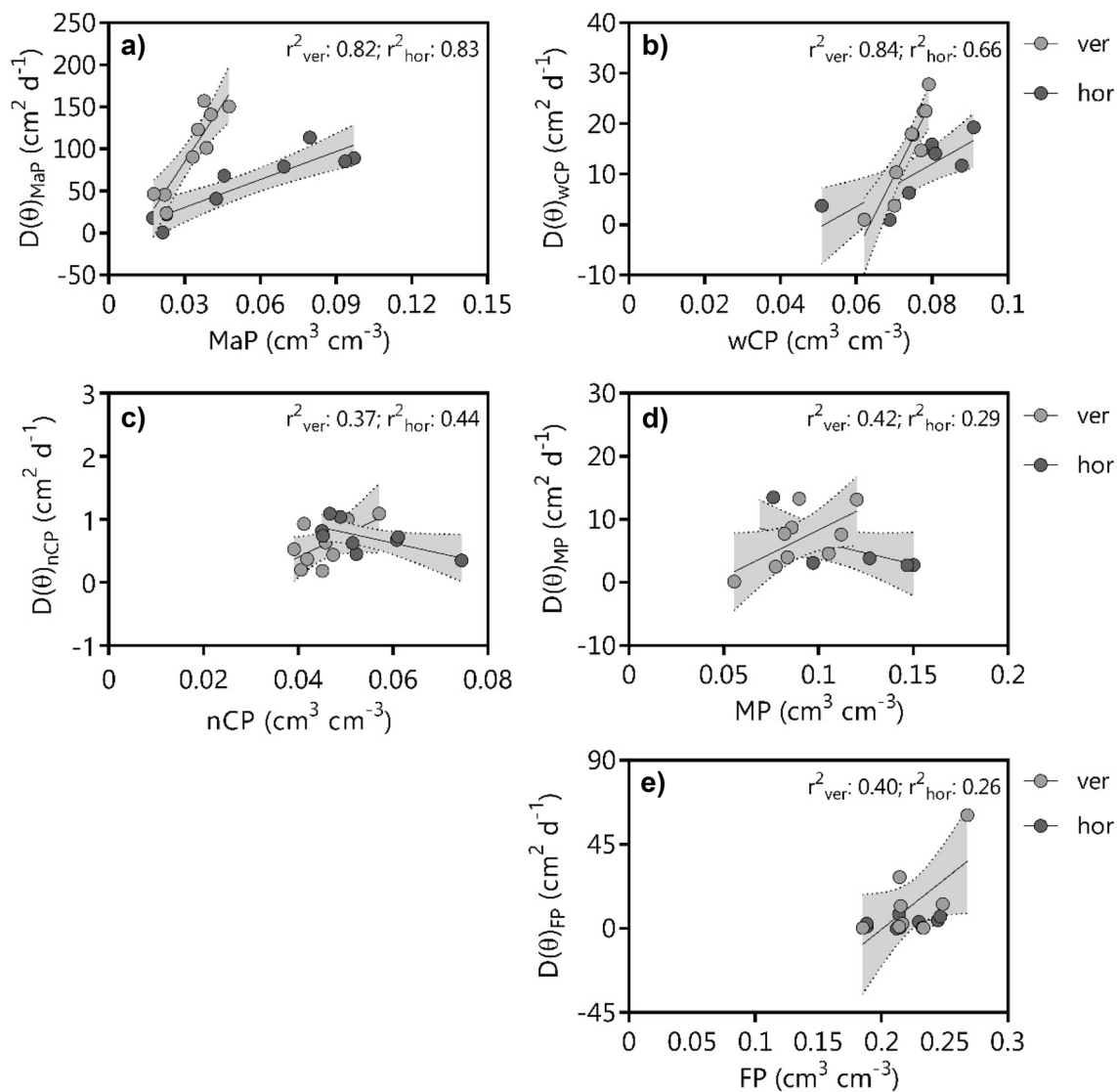


**Fig. 6** Soil water diffusivity,  $D(\theta)$ , as a function of volume fraction of five pore classes: (a) macropores MaP ( $h_1 \geq -10$  hPa), (b) wide coarse pores wCP ( $-10 > h_2 \geq -60$  hPa), (c) narrow coarse pores nCP ( $-60 > h_3 \geq -300$  hPa), (d) medium pores MP ( $-300 > h_4 \geq -15,000$  hPa), and (e) fine pores FP ( $h_5 < -15,000$  hPa).

The dashed lines indicate the confidence intervals of 95% of the relations between the  $D(\theta)$ -values and the pore size distribution (pore size) fitted to 12 data points in vertical (ver) and horizontal (hor) direction, respectively

direction (Alaoui et al. 2011; Beck-Broichsitter et al. 2020a).

It is suggested that the BwC horizon represents a critical part of the hillslope soil profile with hydraulic characteristics favouring generation of subsurface lateral preferential flow at the mountainous Uhlirska catchment, especially during snow melt events and heavy rain storms that provide nearly saturated soil conditions at the base of the soil profile (Sanda and Cislerova 2009; Sanda et al. 2014). In addition, the hillslope provides the slope gradient that is needed for lateral subsurface water flow (Widomski et al. 2015; Beck-Broichsitter et al. 2018). This assumption

is underlined by a study of Wiekenkamp et al. (2016), which confirmed that the spatial and temporal occurrence of subsurface lateral flow is triggered by the amount and intensity of precipitation (Weiler and McDonnell 2004).

It is mentioned by Brooks et al. (2004) that small-scale  $K_s$  values do not represent large scale  $K_s$  value due to a general lack in a necessary number of samples and also not reproduce larger pore networks. By contrast, machine learning algorithms can be used to develop high-performance pedotransfer functions regarding the sensitivity of  $K_s$  values to the soil structure (Araya and Ghezzehei 2019). Thus, large-scale  $K_s$  values from in situ

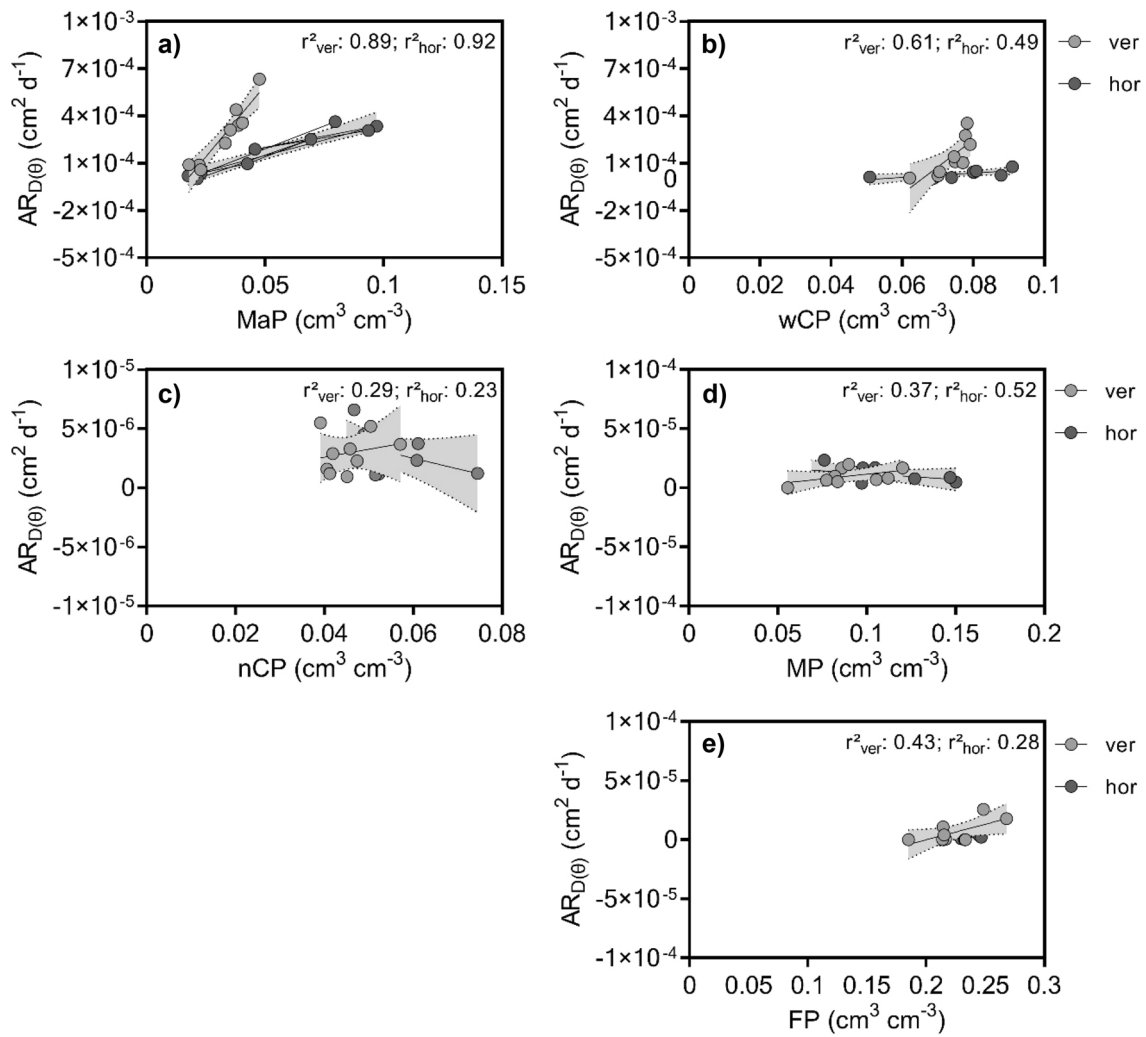
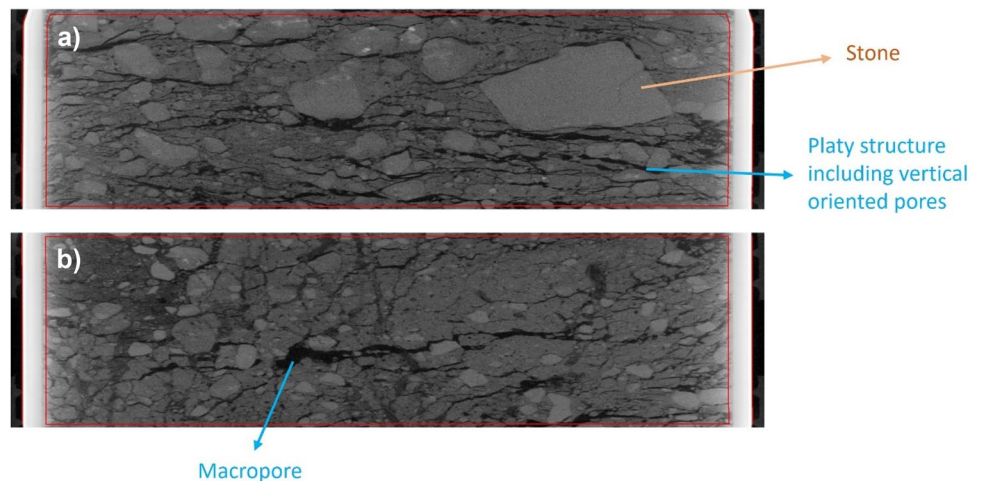


**Fig. 7**  $D(\theta)$ -weighted average anisotropy ratio  $AR_{D(\theta)}$  as a function of the volume fraction of five pore classes: (a) macropores MaP ( $h_1 \geq -10$  hPa), (b) wide coarse pores wCP ( $-10 > h_2 \geq -60$  hPa), (c) narrow coarse pores nCP ( $-60 > h_3 \geq -300$  hPa), (d) medium pores MP ( $-300 > h_4 \geq -15,000$  hPa), and (e) fine pores FP

( $h_5 < -15,000$  hPa). The dashed lines indicate the confidence intervals of 95% of the relations between  $AR_{D(\theta)}$  and the volume fraction of pore classes fitted to 12 data points in vertical (ver) and horizontal (hor) direction, respectively

**Fig. 8** Vertical cross section of automatically detected soil column outlines (red) of CT-based images for the vertical sampled soil core (a) and the horizontal sampled soil core (b) for further validation purposes



experiments can be used for training the algorithms to improve the predicting function of small-scale  $K_s$  values and, therefore, the model-based upscaling performance.

The  $D(\theta)$  as direct link between  $K(\text{Se})$  values and the pore size classes improve the validity for describing pore networks on small scales (Beck-Broichsitter et al. 2020a) compared to standalone  $K_s$  values that can be hardly predicted by pedotransfer functions (Mirus 2015; Pirastru et al. 2017).

### CT image analysis

The process of image segmentation and the pore space analysis using SoilJ (Koestel et al. 2018) show a CT-based macropore volume ( $\text{MaP}_{\text{CT}}$ ) of  $0.028 \text{ cm}^3 \text{ cm}^{-3}$  for the vertical and  $0.047 \text{ cm}^3 \text{ cm}^{-3}$  for the horizontal oriented soil cores (Table 5). The  $\text{MaP}_{\text{CT}}$  values are slightly lower than the mean  $\text{MaP}$  values in Table 2 with  $0.038 \text{ cm}^3 \text{ cm}^{-3}$  and  $0.079 \text{ cm}^3 \text{ cm}^{-3}$ , respectively. The discrepancy was probably caused by different measurement approaches (e.g., Pagenkemper et al. 2013) and a threshold-based underestimation of macropore volume (Koestel 2018; Leue et al. 2020). The CT technique and the used SoilJ software (Koestel et al. 2018) enabled a rapid extraction and quantification of structural features. The critical pore diameter is the bottleneck in the connection from top to bottom and varies between 9.28 vx (vertical) and 9.15 vx (horizontal).

The  $A_{\text{CT}}$  values considering the  $\text{MaP}_{\text{CT}}$  are larger for the horizontal sampled soil core than for the vertical, and both are classified as predominantly isotropic, while the predominant orientation of macropores is  $x$ -axis (=  $y$ -axis) for the vertical and  $z$ -axis for the horizontal oriented soil core and, therefore, parallel to the sampling direction ( $90^\circ$ ). (Fig. 9c, d).

The results in Fig. 9 show that stones and rock fragments form an abandoned and continuous pore network from  $\mu\text{m}$ - to  $\text{mm}$ -scale. It is obviously pore structure which differs from earthworm- and root-derived macropores (e.g., Pagenkemper et al. 2013; Schlüter et al. 2020). Its connectivity depends on the layering and the size of stones and

fragments, and even stones can have some porosity, based on the way they were weathered (e.g., Naseri et al. 2019). The predominant orientation of macropores in  $z$ -axis of the horizontal sampled soil core underlines the findings that weathered bedrock strata can initiate lateral preferential flow especially during intense rainfall events (Dusek and Vogel, 2014). However, further analysis is necessary using the derived results for upscaling of small-scale macropore network information upon the catchment scale as also proposed by Schlüter et al. (2020).

### Anisotropic hydraulic conditions and slope stability

Considering the term soil structure again, anisotropic soil hydraulic properties may help in evaluating slope stability at the hillslope scale in relation to the rainfall characteristics and environmental conditions. Especially soil structure dependent permeability contrasts among soil horizons can impact infiltration processes and the pore water pressure distribution (Zhao and Zhang 2014) resulting in locally diverted flow dynamics (Formetta and Capparelli 2019; Fusco et al. 2021). Soil deformation due to mechanical loads can lead to a distinct horizontal anisotropy of the pore system in the (sub)soil because of anthropogenic induced plate structure formation. Accompanying positive pore water pressures can result in a decrease of the shear strength or an increase in driving forces causing slope instability (Yeh et al. 2015; Hartge and Horn 2016; Fusco et al. 2021). Thus, it becomes obvious, that shear parameters are tensors which depend on the aggregation besides all further internal properties (Dörner and Horn 2009).

However, additional research is needed to combine anisotropy of soil hydraulic and mechanical properties for evaluation slope stability under various soil and vegetation types.

### Conclusion

The results of this study indicate direction-dependent differences in the soil hydraulic conductivity as function of effective saturation,  $K(\text{Se})$ . The soil water diffusivity,  $D(\theta)$ , as link between the intensity and capacity parameter was found to strongly depend on the pore size distribution. Thus, by weighting the anisotropy ratio with the soil water diffusivity, both the capacity and the intensity parameters were combined. The analysed X-ray CT images indicate that more pronounced cracks were observed in the soil samples taken in horizontal than in vertical direction in the BwC horizon of hillslope profile.

The anisotropy in the range of the soil macropores was determined, resulting in increased value of hydraulic conductivity in the horizontal direction. Similar trend was found

**Table 5** Results of the CT image analysis for the vertical (ver) and horizontal (hor) sampled soil core using SoilJ (Koestel 2018)

Direction	$\text{MaP}_{\text{CT}}$	$A_{\text{CT}}$	$d_{\text{crit}}$	Predominant orientation
	$\text{cm}^3 \text{ cm}^{-3}$	–	vx	–
ver	0.028	0.09	9.28	$x$ -axis
hor	0.047	0.31	9.15	$z$ -axis

Volume of macropores ( $\text{MaP}_{\text{CT}}$ :  $d > 1.134$  pixel) as ratio between phase volume (voxel) and bulk volume (voxel) of the ROI, CT-based anisotropy ratio  $A_{\text{CT}}$ , critical diameter,  $d_c$  (vx), and predominant orientation of macropores ( $x$ ,  $y$ ,  $z$  direction)

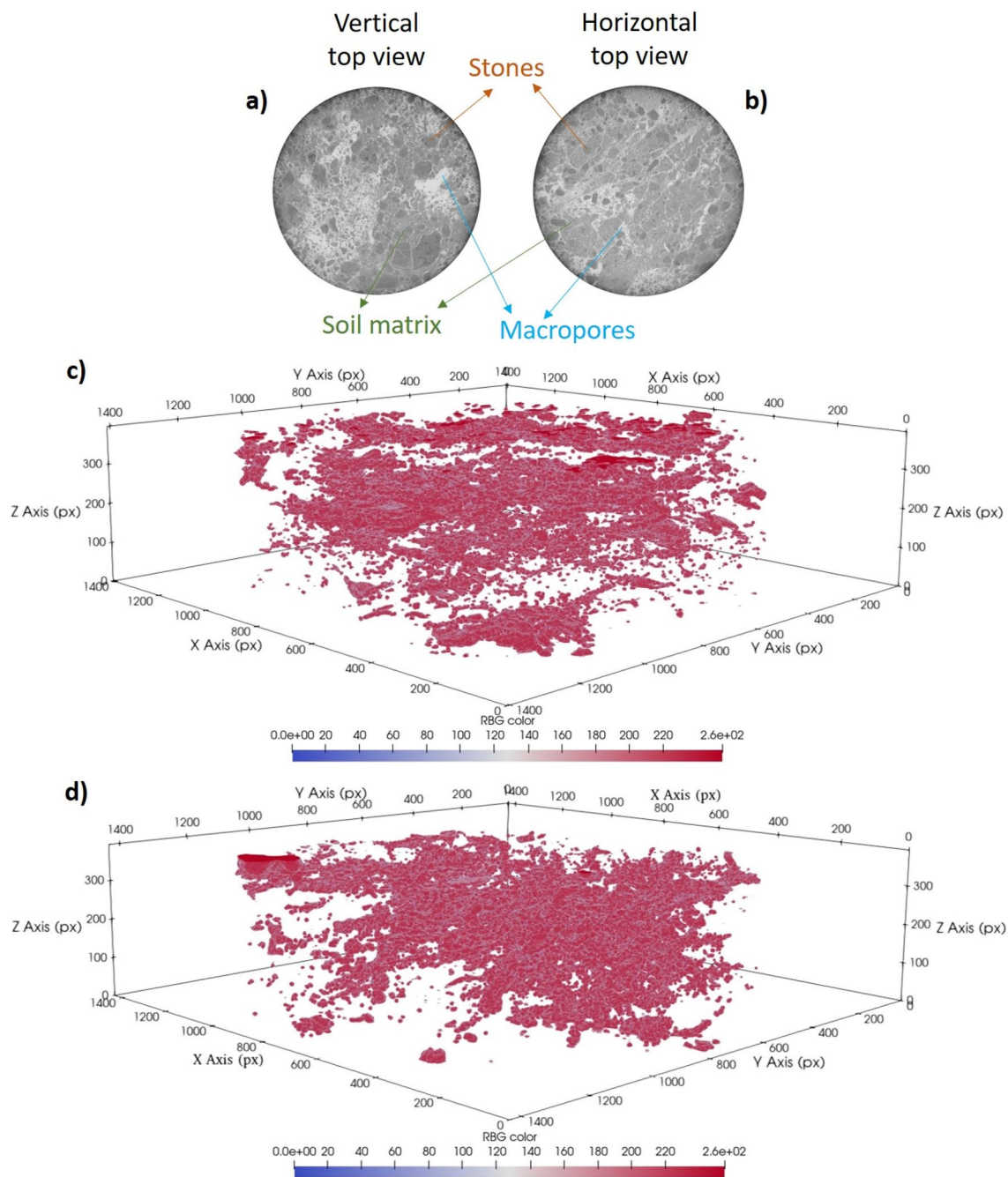


**Fig. 9** 2D images (8bit) of the top view (**a**, **b**) for vertical ( $0^\circ$ ) and horizontal ( $90^\circ$ ) sampled soil cores (height: 5.5 cm; diameter: 8 cm). 3D images of the vertical (**c**) and horizontal (**d**) samples. The 3D views of the vertical (**c**) and horizontal (**d**) oriented macropore volume ( $d > 1.134$  pixel) with an image resolution of  $1407 \times 1407$  pixel

in  $x/y$  extent and 395 pixels in  $z$  extent, respectively. The 3D images were created with the visualisation software Paraview (e.g., Ahrens et al. 2005). Color's RGB values  $> 200$  indicate pores with diameter  $> 1$  mm ( $\sim 3.8$  pixel)

for the medium pores. In the current study, the anisotropy ratios above 1 in the volume fraction of the macropores close to saturation indicate exemplary the tendency of the BwC horizon of the Dystric Cambisol for supporting the subsurface lateral water flow of the mountainous hillslopes Uhlirska catchment. Based on the study results, the refined

information on soil hydraulic characteristics have the potential to improve runoff predictions at the hillslope scale. The X-ray computer tomography-based anisotropy ratio is larger for the horizontal sampled soil core than for the vertical, and both are classified as predominantly isotropic. However, the predominant orientation of macropores in  $z$ -axis of the

horizontally sampled soil core and, therefore, parallel to the sampling direction (90°) underlines the findings that weathered bedrock strata can initiate lateral preferential flow.

In future, the small-scale direction-dependent differences in the soil hydraulic capacity and intensity parameter will be used for model-based upscaling for better understanding of preferential flow at the catchment scale.

**Funding** Open Access funding enabled and organized by Projekt DEAL. This study was funded by the Czech Science Foundation, project 20-00788S. The authors thank Ines Schütt (University Kiel) for the soil chemical analysis. The authors thank John Koestel (Swedish University of Agricultural Sciences, Uppsala) for its support with the SoilJ software.

## Declarations

**Conflict of interest** The authors have not disclosed any competing interests.

**Open Access** This article is licensed under a Creative Commons Attribution 4.0 International License, which permits use, sharing, adaptation, distribution and reproduction in any medium or format, as long as you give appropriate credit to the original author(s) and the source, provide a link to the Creative Commons licence, and indicate if changes were made. The images or other third party material in this article are included in the article's Creative Commons licence, unless indicated otherwise in a credit line to the material. If material is not included in the article's Creative Commons licence and your intended use is not permitted by statutory regulation or exceeds the permitted use, you will need to obtain permission directly from the copyright holder. To view a copy of this licence, visit <http://creativecommons.org/licenses/by/4.0/>.

## References

- Ahrens J, Geveci B, Law C (2005) ParaView: an end-user tool for large data visualization, visualization handbook 2005. Elsevier, Amsterdam, pp 717–731. <https://doi.org/10.1016/B978-012387582-2/50038-1>
- Alaoui A, Lipiec J, Gerke HH (2011) A review of the changes in the soil pore system due to soil deformation: a hydrodynamic perspective. *Soil till Res* 115–116:1–15. <https://doi.org/10.1016/j.still.2011.06.002>
- Araya S, Ghezzehei TA (2019) Using machine learning for prediction of saturated hydraulic conductivity and its sensitivity to soil structural perturbations. *Water Resour Res*. <https://doi.org/10.1029/2018WR024357>
- Beck-Broichsitter S, Gerke HH, Horn R (2018) Assessment of leachate production from a municipal solid-waste landfill through water-balance modeling. *Geosciences* 8(10):372. <https://doi.org/10.3390/geosciences8100372>
- Beck-Broichsitter S, Fleige H, Dusek J, Gerke HH (2020a) Anisotropy of unsaturated hydraulic properties of compacted mineral capping systems seven years after construction. *Soil till Res* 204:104702. <https://doi.org/10.1016/j.still.2020.104702>
- Beck-Broichsitter S, Gerke HH, Leue M, von Jeetze PJ, Horn R (2020b) Anisotropy of unsaturated soil hydraulic properties of eroded Luvisol after conversion to hayfield comparing alfalfa and grass plots. *Soil till Res* 198:104553. <https://doi.org/10.1016/j.still.2019.104553>
- Beck-Broichsitter S, Fleige H, Gerke HH, Horn R (2020c) Effect of artificial soil compaction in landfill capping systems on anisotropy of air-permeability. *J Plant Nutr Soil Sci* 183(2):144–154. <https://doi.org/10.1002/jpln.201900281>
- Beck-Broichsitter S, Gerriets MR, Neumann M, Kubat J-F, Dusek J (2022) Spatial particle size distribution at intact sample surfaces of a Dystric Cambisol under forest use. *J Hydrol Hydromech* 70(1):1–12. <https://doi.org/10.2478/johh-2022-0003>
- Brooks ES, Boll J, McDaniel PA (2004) A hillslope-scale experiment to measure lateral saturated hydraulic conductivity. *Water Resour Res*. <https://doi.org/10.1029/2003WR002858>
- Carminati A, Kaestner A, Hassanein R, Ippisch O, Vontobel P, Flüher H (2007) Infiltration through series of soil aggregates: neutron radiography and modelling. *Adv Water Resour* 30(5):1168–1178
- Chandrasekhar P, Kreiselmeier J, Weninger T, Julich S, Feger K-H, Schwen A, Schwärzel K (2019) Modeling the evolution of soil structural pore space in agricultural soils following tillage. *Geoderma* 353:401–414. <https://doi.org/10.1016/j.geoderma.2019.07.017>
- DIN 18130-1 (1998) Soil—investigation and testing; determination of the coefficient of water permeability—part 1: laboratory tests. Beuth Verlag GmbH, Berlin
- Ding D, Zhao Y, Feng H, Peng X, Si B (2016) Using the double-exponential water retention equation to determine how soil pore-size distribution is linked to soil texture. *Soil till Res* 156:119–130. <https://doi.org/10.1016/j.still.2015.10.007>
- Dohnal M, Vogel T, Sanda M, Jelinkova V (2012) Uncertainty analysis of a dual-continuum model used to simulate subsurface hillslope runoff involving oxygen-18 as natural tracer. *J Hydrol Hydromech* 60(3):194–205. <https://doi.org/10.2478/v10098-012-0017-0>
- Dörner J, Horn R (2009) Direction-dependent behavior of hydraulic and mechanical properties in structured soils under conventional and conservational tillage. *Soil till Res* 102:225–232. <https://doi.org/10.1016/j.still.2008.07.004>
- Doube M, Klosowski MM, Arganda-Carreras I, Cordelieres FP, Dougherty RP, Jackson JS, Schmid B, Hutchinson JR, Shefelbine SJ (2010) BoneJ: free and extensible bone image analysis in ImageJ. *Bone* 47:1076–1079. <https://doi.org/10.1016/j.bone.2010.08.023>
- Durner W (1994) Hydraulic conductivity estimation for soils with heterogeneous pore structure. *Water Resour Res* 26:1483–1496. <https://doi.org/10.1029/93WR02676>
- Dusek J, Vogel T (2014) Modeling subsurface hillslope runoff dominated by preferential flow: one- vs. two-dimensional approximation. *Vadose Zone J*. <https://doi.org/10.2136/vzj2013.05.0082>
- Dusek J, Vogel T (2016) Hillslope-storage and rainfall-amount thresholds as controls of preferential stormflow. *J Hydrol* 534:590–605. <https://doi.org/10.1016/j.jhydrol.2016.01.047>
- Dusek J, Vogel T (2018) Hillslope hydrograph separation: the effects of variable isotopic signatures and hydrodynamic mixing in macroporous soil. *J Hydrol* 563:446–459. <https://doi.org/10.1016/j.jhydrol.2018.05.054>
- Dusek J, Vogel T (2019) Modeling travel time distributions of preferential subsurface runoff, deep percolation and transpiration at a montane forest hillslope site. *Water* 11:2396. <https://doi.org/10.3390/w11112396>
- FAO (2006) Guidelines for soil description. FAO-ISRIC Press, Rome
- Feldkamp LA, Davis LC, Kress JW (1984) Practical conebeam algorithm. *J Opt Soc Am* 1:612–619. <https://doi.org/10.1364/JOSAA.1.000612>
- Formetta G, Capparelli G (2019) Quantifying the three-dimensional effects of anisotropic soil horizons on hillslope hydrology and stability. *J Hydrol* 570:329–342. <https://doi.org/10.1016/j.jhydrol.2018.12.064>

- Fusco F, Mirus BB, Baum RL, Calcaterra D, de Vita P (2021) Incorporating the effects of complex soil layering and thickness local variability into distributed landslide susceptibility assessments. *Water* 13(5):713. <https://doi.org/10.3390/w13050713>
- Germer K, Braun J (2015) Determination of anisotropic saturated hydraulic conductivity of a macroporous slope soil. *Soil Sci Soc Am J* 79:1528–1536. <https://doi.org/10.2136/sssaj2015.02.0071>
- Godefroid S, Koedam N (2010) Tree-induced soil compaction in forest ecosystems: myth or reality? *Eur J Forest Res* 129:209–217. <https://doi.org/10.1007/s10342-009-0317-z>
- Guo L, Chen J, Lin H (2014) Subsurface lateral preferential flow network revealed by time-lapse ground-penetrating radar in a hillslope. *Water Resour Res* 50(12):9127–9147. <https://doi.org/10.1002/2013WR014603>
- Hansson L, Koestel J, Ring E, Gärdenas A (2017) Impacts of off-road traffic on soil physical properties of forest clear-cuts: X-ray and laboratory analysis. *Scand J for Res* 33(2):166–177. <https://doi.org/10.1080/02827581.2017.1339121>
- Hartge KH, Horn R (2016) Essential soil physics—an introduction to soil processes, structure, and mechanics. In: Horton R, Horn R, Bachmann J, Peth S (eds) Schweizerbart Science Publishers, Stuttgart
- Hillel D (1998) Environmental soil physics. Academic Press, Waltham, New York
- Horn R, Kutilek M (2009) The intensity–capacity concept—how far is it possible to predict intensity values with capacity parameters. *Soil Till Res* 103:1–3. <https://doi.org/10.1016/j.still.2008.10.007>
- Horn R, Peng X, Fleige H, Dörner J (2014) Pore rigidity in structured soils—only a theoretical boundary condition for hydraulic properties? *Soil Sci Plant Nutr* 60:3–14. <https://doi.org/10.1080/00380768.2014.886159>
- Horn R, Mordhorst A, Fleige H, Zimmermann I, Burbaum B, Filipinski M, Cordens E (2019) Soil Type and land use effects on tensorial properties of saturated hydraulic conductivity in Northern Germany. *J Soil Sci* 71(2):179–189. <https://doi.org/10.1111/ejss.12864>
- Hurvich CM, Tsai CL (1989) Regression and time series model selection in small sample. *Biometrika* 76(2):99–104. <https://doi.org/10.1093/biomet/76.2.297>
- IUSS Working Group WRB. 2015. World Reference Base for Soil Resources 2014, update 2015. International soil classification system for naming soils and creating legends for soil maps. World Soil Resources Reports No. 106. FAO, Rome.
- Klatt MA, Schröder-Turk GE, Mecke K (2017) Mean-intercept anisotropy analysis of porous media. II. Conceptual shortcomings of the MIL tensor definition and Minkowski tensors as an alternative. *Med Phys* 44(7):3663–3675. <https://doi.org/10.1002/mp.12280>
- Koestel J (2018) SoilJ—an ImageJ plugin for the semi-automatic processing of 3-D X-ray images of soils. *Vadose Zone J* 17:170062. <https://doi.org/10.2136/vzj2017.03.0062>
- Legland D, Arganda-Carreras I, Andrey P (2016) MorphoLibJ: integrated library and plugins for mathematical morphology with ImageJ. *Bioinformatics (Oxford Univ Press)* 32(22):3532–3534. <https://doi.org/10.1093/bioinformatics/btw413> (PMID 27412086)
- Leue M, Uteau D, Peth S, Beck-Broichsitter S, Gerke HH (2020) Volume-related quantification of organic carbon content and cation exchange capacity of macropore surfaces in Bt horizons. *Vadose Zone J* 19(1):e20069. <https://doi.org/10.1002/vzj2.20069>
- Mehra OP, Jackson ML (1960) Iron oxide removal from soils and clays by a dithionite-citrate system buffered with sodium bicarbonate. *Clay Clay Miner* 7:317–327. <https://doi.org/10.1346/CCMN.1958.0070122>
- Mirus BB (2015) Evaluating the importance of characterizing soil structure and horizons in parameterizing a hydrologic process model. *Hydrol Process* 29(21):4611–4623. <https://doi.org/10.1002/hyp.10592>
- Naseri M, Iden SC, Richter N, Durner W (2019) Influence of stone content on soil hydraulic properties: experimental investigation and test of existing model concepts. *Vadose Zone J* 18(1):1–10. <https://doi.org/10.2136/vzj2018.08.0163>
- Odgaard A (1997) Three-dimensional methods for quantification of cancellous bone architecture. *Bone* 20(4):315–328. [https://doi.org/10.1016/S8756-3282\(97\)00007-0](https://doi.org/10.1016/S8756-3282(97)00007-0)
- Otsu N (1979) A threshold selection method from gray-level histograms. *IEEE Trans Syst Man Cybern* 9:62–66. <https://doi.org/10.1109/TSMC.1979.4310076>
- Pagenkemper SK, Peth S, Uteau-Puschmann D, Horn R (2013) Effects of root-induced biopores on pore space architecture investigated with industrial X-ray computed tomography. In: Anderson SH, Hopmans JW (eds) Soil-water-root processes: advances in tomography and imaging, vol 61. SSSA, Madison. <https://doi.org/10.2136/sssaspecpub61.c4>
- Paradelo Perez M, Katuwal S, Moldrup P, Norgaard T, Herath L, de Jonge LW (2016) X-ray CT-derived soil characteristics explain varying air, water, and solute transport properties across a loamy field. *Vadose Zone J* 15(4):vzj2015.07.0104. <https://doi.org/10.2136/vzj2015.07.0104>
- Pertassek T, Peters A, Durner W (2015) HYPROP-FIT software user's manual, V.3.0, UMS GmbH, Gmunder Str. 37, 81379 München, Germany
- Pirastu M, Bagarello V, Iovino M, Marrosu R, Castellini M, Giadrossich F, Niedda M (2017) Subsurface flow and large-scale lateral saturated soil hydraulic conductivity in a Mediterranean hillslope with contrasting land uses. *J Hydrol Hydromech.* <https://doi.org/10.1515/johh-2017-0006>
- Priesack E, Durner W (2006) Closed-form expression for the multimodal unsaturated hydraulic conductivity. *Vadose Zone J* 5:121–124. <https://doi.org/10.2136/vzj2005.0066>
- Sanda M, Cislerova M (2009) Transforming hydrographs in the hillslope subsurface. *J Hydrol Hydromech* 57:264–275. <https://doi.org/10.2478/v10098-009-0023-z>
- Sanda M, Vitvar T, Kulasova A, Jankovec J, Cislerova M (2014) Run-off formation in a humid, temperate headwater catchment using a combined hydrological, hydrochemical and isotopic approach (Jizera Mountains, Czech Republic). *Hydrol Process* 28:3217–3229. <https://doi.org/10.1002/hyp.9847>
- Schindler U (1980) Ein Schnellverfahren zur Messung der Wasserleitfähigkeit im teilgesättigten Boden an Stechzylinderproben. *Arch Acker Pflanzenbau Bodenkd* 24:1–7
- Schindler U, Durner W, von Unold G, Müller L (2010) Evaporation method for measuring unsaturated hydraulic properties of soils: extending the measurement range. *Soil Sci Soc Am J* 74(4):1071–1083. <https://doi.org/10.2136/sssaj2008.0358>
- Schlüter S, Albrecht L, Schwärzel K, Kreiselmeier J (2020) Long-term effects of conventional tillage and no-tillage on saturated and near-saturated hydraulic conductivity—can their prediction be improved by pore metrics obtained with X-ray CT? *Geoderma* 361:114082. <https://doi.org/10.1016/j.geoderma.2019.114082>
- Schneider CA, Rasband WS, Eliceiri KW (2012) NIH Image to ImageJ: 25 years of image analysis. *Nat Methods* 9:671–675. <https://doi.org/10.1038/nmeth.2089>
- UMS GmbH Munich. 2015. Manual HYPROP, Version 2015–01, 96 pp. UMS GmbH, Gmunder Straße 37, Munich, Germany. URL [http://ums-muc.de/static/Manual\\_HYPROP.pdf](http://ums-muc.de/static/Manual_HYPROP.pdf). Accessed 20 Mar 2021
- van Genuchten MT (1980) A closed-form equation for predicting the hydraulic conductivity of unsaturated soils. *Soil Sci Soc Am J* 44:892–898. <https://doi.org/10.2136/sssaj1980.03615995004400050002x>
- Weiler M, McDonnell J (2004) Virtual experiments: a new approach for improving process conceptualization in hillslope hydrology. *J*

- Hydrol 285(1–4):3–18. [https://doi.org/10.1016/S0022-1694\(03\)00271-3](https://doi.org/10.1016/S0022-1694(03)00271-3)
- Weiler M, McDonnell JJ (2007) Conceptualizing lateral preferential flow and flow networks and simulating the effects on gauged and ungauged hillslopes. *Water Resour Res*. <https://doi.org/10.1029/2006WR004867>
- Weiler M, McGlynn BL, Mcguire KJ, McDonnell JJ (2003) How does rainfall become runoff? A combined tracer and runoff transfer function approach. *Water Resour Res* 227(2):1015–1029. <https://doi.org/10.1029/2003WR002331>
- Wendroth O, Ehlers W, Hopmans JW, Klage H, Halbertsma J, Woesten JHM (1993) Reevaluation of the evaporation method for determining hydraulic functions in unsaturated soils. *Soil Sci Soc Am J* 57:1436–1443. <https://doi.org/10.2136/sssaj1993.03615995005700060007x>
- Weninger T, Bodner G, Kreiselmeier J, Chandrasekhar P, Julich S, Feger K-H, Schwärzel K, Schwen A (2018) Combination of measurement methods for a wide-range description of hydraulic soil properties. *Water* 10(8):1021. <https://doi.org/10.3390/w10081021>
- Widomski MK, Beck-Broichsitter S, Zink A, Fleige H, Horn R, Stepniewski W (2015) Numerical modeling of water balance of temporary landfill cover in Northern Germany. *J Plant Nutr Soil Sci* 178(3):401–412. <https://doi.org/10.1002/jpln.201400045>
- Wiekenkamp I, Huisman JA, Bogena HR, Lin HS, Vereecken H (2016) Spatial and temporal occurrence of preferential flow in a forested headwater catchment. *J Hydrol* 534:139–149. <https://doi.org/10.1016/j.jhydrol.2015.12.050>
- Xu P, Zhang Q, Qian H, Hou K (2020) Investigation into microscopic mechanisms of anisotropic saturated permeability of undisturbed  $Q_2$  loess. *Environ Earth Sci* 79(18):420. <https://doi.org/10.1007/s12665-020-09152-7>
- Xu P, Lin T, Qian H, Zhang Q (2021) Anisotropic microstructure of loess-paleosol sequence and its significance for engineering and paleoclimate: a case study from Xiushidu (XSD) profile, southern Chinese Loess Plateau. *Eng Geol* 286(5):106092. <https://doi.org/10.1016/j.enggeo.2021.106092>
- Yeh HF, Wang J, Shen KL, Lee CH (2015) Rainfall characteristics for anisotropic conductivity of unsaturated soil slopes. *Environ Earth Sci* 73(12):8669–8681. <https://doi.org/10.1007/s12665-015-4032-4>
- Zhang Z, Peng X (2021) Bio-tillage: a new perspective for sustainable agriculture. *Soil till Res* 206:104844. <https://doi.org/10.1016/j.still.2020.104844>
- Zhao HF, Zhang LM (2014) Instability of saturated and unsaturated coarse granular soils. *J Geotech Geoenviron* 140:25–35. [https://doi.org/10.1061/\(ASCE\)GT.1943-5606.0000976](https://doi.org/10.1061/(ASCE)GT.1943-5606.0000976)

**Publisher's Note** Springer Nature remains neutral with regard to jurisdictional claims in published maps and institutional affiliations.